

Arbeit zur Erlangung des akademischen Grades  
Master of Science

# Alignment studies for the LHCb SciFi Detector

Nils Breer  
geboren in Unna

2022

Lehrstuhl für Experimentelle Physik IV  
Fakultät Physik  
Technische Universität Dortmund

Erstgutachter:	Prof. Dr. Albrecht
Zweitgutachter:	Prof. Dr. Weingarten
Abgabedatum:	May 4th 2022

## Abstract

The LHCb detector is receiving an upgrade that began in 2019 in the form of a long shutdown of the LHC. The three track detectors behind the dipole magnets have been replaced with a detector that uses scintillating fibers (SciFi). This is only part of the upgrade. Due to larger luminosities and the number of trace multiplicities, detectors with finer granularity are needed. The calibration of the new detector to the software regarding orientation and position is critical for the subsequent performance. This process is called *alignment*.

In this work, the software *alignment* of the SciFi tracker is studied. By testing different parameter configurations a good alignment could be achieved. So called *misalignment* tests contributed to the to determine the quality of the alignment. In addition, tests for the identification of weak modes were performed. This drew attention to a bias within the clusters which has important influence on the alignment.

## Kurzfassung

Der LHCb-Detektor erhält ein Upgrade welches in 2019 in Form eines Long Shut-downs des LHC begann. Die drei Spurdetektoren hinter den Dipolmagneten wurden durch einen Detektor ausgetauscht, welcher szintillierende Fasern verwendet (Sci-Fi). Dies ist nur ein Teil des Upgrades. Aufgrund von größeren Luminositäten und der steigenden Anzahl an Spurmultiplicitäten werden Detektoren mit feinerer Granularität benötigt. Die Kalibrierung des neuen Detektors mit der Software in Orientierung und Position ist entscheidend für die spätere Leistung. Dieser Vorgang heißt *Alignment*.

In dieser Arbeit wird das Software-*Alignment* des SciFi-Trackers studiert. Durch Tests verschiedener Parameter Konfigurationen konnte ein gutes Alignment erreicht werden. Sogenannte *Misalignment*-Tests trugen dazu bei die Qualität des Alignments zu bestimmen. Außerdem wurden Tests zur Identifikation von schwachen Moden durchgeführt. Dies machte auf einen Bias innerhalb der Cluster aufmerksam welcher einen nicht-unwichtigen Einfluß auf das Alignment hat.

# Inhaltsverzeichnis

<b>1</b>	<b>Introduction</b>	<b>1</b>
<b>2</b>	<b>Particles and The Large Hadron Collider</b>	<b>2</b>
2.1	The Standard Modell . . . . .	2
2.2	particle decays and hadrons . . . . .	5
2.3	The LHC and LHCb . . . . .	5
<b>3</b>	<b>The Theory of Alignment</b>	<b>10</b>
3.1	Track Reconstruction . . . . .	10
3.2	The Kalman filter method [15] . . . . .	12
3.3	alignment using derivatives . . . . .	14
<b>4</b>	<b>Alignment of the SciFi</b>	<b>15</b>
4.1	Nulltests and software tests . . . . .	16
4.2	chi2 tests and weak modes . . . . .	27
4.3	luminosity samples and chi2 . . . . .	31
4.4	impact of the cluster bias . . . . .	32
<b>5</b>	<b>Continuing Work</b>	<b>37</b>
<b>6</b>	<b>Future Work</b>	<b>38</b>
<b>7</b>	<b>Conclusion and Outlook</b>	<b>39</b>
	<b>Literatur</b>	<b>40</b>



# 1 Introduction

The beginning of the 20<sup>th</sup> century many physicists started research on elementary particles and the interactions associated with them. The combined knowledge lead to the construction of most precisely tested theories: the Standard Model (SM) of particles. To this day the measurements are in agreement with the model within the theoretical and experimental uncertainties. The SM describes every fundamental force except for gravity. There are still open questions such the matter-antimatter asymmetry in the universe leading to a larger charge-parity (CP) violation than the SM predicted. To tackle these problems, high energy experiments such as the LHCb located at the Large Hadron Collider (LHC) at CERN were build for this exact reason. The LHCb's main purposes are beauty-quark and charm-quark physics especially precision measurements with a focus on decays involving these quarks. These measurements provide insights into CP-violation for massive particle decays. To detect these phenomena the threshold for statistical uncertainties has to be lowered and the amount of data collected needs to be increased. The upgrade described in section 2.3.2 will increase the instantaneous luminosity by a factor of five to  $2 \cdot 10^{33} \text{ fb}^{-1}$  and the detector readout rate will be at 40 MHz. To realize these hardware challenges the frontend electronics and tracking systems needed upgrades. To operate the upgraded Tracker at its full potential the software must be calibrated as good as possible to the physical detector.

The Alignment theory will be described in 3. In chapter different sets of constraints, degrees of freedom and alignable objects called *configuration* will be tested first in order to study how different configurations influence the alignment. Afterwards several tests will be performed to analyse the behavior of a misaligned detector and check if the chosen configuration converges towards an aligned state. Since the detector cannot be aligned the whole time, it is crucial that misalignments do not stay permanent but can be reverted. The LHC will not run permanently at maximum luminosity therefore tests are performed to analyse alignment of different luminosity samples. During the alignment studies a bias inside the clustering algorithms was discovered which had an impact on the alignment. The exact changes will be discussed in the final section of chapter 4.

## 2 Particles and The Large Hadron Collider

Whenever a new detector is build the position where it is physically mounted is roughly where it should be. In order to check this, survey measurements are performed to check the position with a precision of 100  $\mu\text{m}$ . To achieve an even bigger precision, *software alignments* are performed.

The reason why alignment is of great importance is that a misaligned detector yields large momentum resolutions, low reconstruction efficiencies and wrong mass estimations. The most prominent area of misalignment is asymmetries for a spectrometer. In the past, alignment solved problems for example a Muon asymmetry in the L0Muon trigger in 2011 and a misalignment in IT boxes which resulted in trigger inefficiency regarding  $J/\Psi$  in 2012.

With good alignment, studies on all standard modell particles and hadron states will improve. Yielding better efficiencies on SM particle measurements will result in deeper insights regarding physics beyond the stand modell from high-precision measurements of CP-violating observables as an example.

On a grand scheme upgrading the LHCb and therefore the LHC will bring deeper insights "for" (wrong word) standard model processes. To understand the universe even better and eventually yield information about the unsolved question of "dark matter" and "dark energy", what is believed to be the bulk of the universes content.

### 2.1 The Standard Modell

The standard model of particle physics<sup>2.1</sup> describes the known elementary particles and their interactions. It consists of 12 matter particles, the fermions and five interaction particles, which are called vector bosons.

The fermions 12 spin- $\frac{1}{2}$  particles. Six are called leptons and they are sorted into three families, also called flavors (e,  $\mu$  and  $\tau$ ) and six are called quarks. Each of those lepton families has a charged lepton<sup>1</sup> and a left-handed neutrino. A particle is called left-handed if its spin direction is opposite to the direction of flight. Right-handed particles have a spin direction pointing with the direction of flight. Neutrinos can

---

<sup>1</sup>can have both händigkeiten



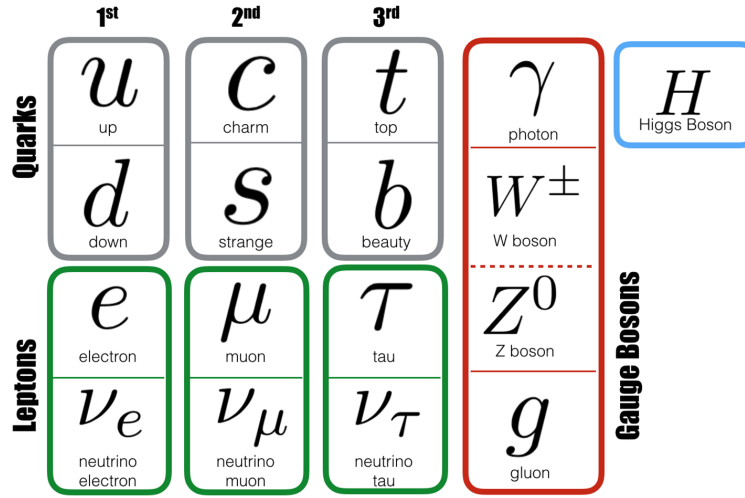


Abbildung 2.1: The standard model of particle physics[11].

only be left-handed since there is no system where the neutrino can be "overtaken" so the momentum switches and therefore the helicity. A left-handed isospin doublet and a left-handed singlet can be constructed. The leptons can couple via the weak-interaction and if they are charged, also via the em-interaction. Neutrinos can only couple via the weak interaction. Each matter particle also has an antiparticle, with an opposite charge.

The quarks are spin- $\frac{1}{2}$ -fermions and carry an electric charge as well. In each of the three generations there is one isospin doublet. The quarks are ordered by ascending mass. In the first generation are the two lightest quarks, up- and down quark, in the second generation the charm- and strange quark and in the third generation the top- and bottom quark doublet. Quarks carry a color charge, red, green or blue, which is an artificially introduced degree of freedom to guarantee the distinguishability.

The interactions are obtained from the vector bosons mentioned above. The three potent interactions are the electromagnetic(em) interaction, the weak interaction and the strong interaction. Gravitation does not make a significant contribution. The vector boson of the em interaction is the photon which is exchanged between particles. The strength of one of those interactions is described by a coupling constant. In the em interaction this is the fine structure constant[9]. The range of the em-interaction is in principle infinite, but decreases with increasing distance between the interacting particles. The em interaction is described by quantum electrodynamics. The potentials are described by operators, which create and annihilate the photons.

The exchange particles of the weak interaction are on the one hand the  $W^\pm$ -bosons and on the other hand the Z-boson. The weak interaction processes are called currents. Changing the charge during the interaction by a W-boson is called charged current. The exchange reaction of a Z boson in, for example, processes such as  $e_\nu\mu \rightarrow e_\nu\mu$  is called neutral current. Analogous to the electromagnetic interaction, the potentials are again understood as operators, but here there are no propagators. Propagators are used in *FEYNMAN*-diagrams of QED to represent the interaction particles. A so-called V-A structure is used here instead. Here, V stands for vectorboson and A is the axialvector. This structure is needed to disregard the right-handed particles and left-handed antiparticles, since these lead to the charge-parity violation. Thus the Lorentz factors are adjusted in the following way

$$\gamma_\mu \rightarrow \gamma_\mu(1 - \gamma_5)$$

Quarks couple via the strong interaction which is described by the quantum chromodynamic (QCD). The Eichgroup of the QCD is  $SU(N = 3)$  where N is the number of introduced colors as a new degree of freedom. The number of generators is therefore  $N^2 - 1 = 8$ . The generators are called gluons and they carry color and anticolor, have no mass and carry spin 1. Gluons can, other than photons, couple to themselves. Moreover, the coupling constant  $\alpha_s \approx 0.1$ . The interaction with quarks is described with a potential.

$$V_{q\bar{q}} = -\frac{4\alpha_s}{3r} + \sigma \cdot r \quad (2.1)$$

with

$$\sigma = 1 \frac{\text{GeV}}{\text{fm}} \quad (2.2)$$

The common eight gluon-wavefunctions[14] are

$$\begin{aligned} \psi_1 &= |r\bar{g}\rangle & \psi_2 &= |r\bar{b}\rangle \\ \psi_3 &= |g\bar{r}\rangle & \psi_4 &= |g\bar{b}\rangle \\ \psi_5 &= |b\bar{r}\rangle & \psi_6 &= |b\bar{g}\rangle \\ \psi_7 &= \frac{1}{\sqrt{2}}(|r\bar{r}\rangle - |g\bar{g}\rangle) & \psi_8 &= \frac{1}{\sqrt{6}}(|r\bar{r}\rangle + |g\bar{g}\rangle - 2|b\bar{b}\rangle) \end{aligned}$$

The second wavefunction describes a gluon interaction with a blue quark and changing the color to red.

Quarks thus tend to attract each other very strongly. If now quark and anti quark are moved away from each other, a lot of energy has to be expended. This energy can become so large that new particles can be created.

Due to the Confinement, quarks cannot exist alone. Instead they form bonding states, so called hadrons. On the one hand there are the mesons, which consist of a quark and an antiquark.

$$|M\rangle = |q\bar{q}'\rangle \quad (2.3)$$

These may be from the same family (i.e. [u,d], [c,s], [t,b]), or from different families. Mesons have a baryon number of 0. Accordingly, quarks carry the baryon number  $\frac{1}{3}$ . The quarks constructing a meson therefore carries color and the corresponding anticolor. The second type are baryons. The content consists of either three quarks or three antiquarks. However, it cannot be that one quark and two antiquarks and vice versa occur, because baryons must have the baryon number  $B = 1$ . Because baryons are stable final states as well as the mesons, the sum of their quark colors must be white. Therefore, every (anti)color must occur once in a baryon.

$$|B\rangle = |qq'q''\rangle \quad (2.4)$$

$$|\bar{B}\rangle = |\bar{q}\bar{q}'\bar{q}''\rangle \quad (2.5)$$

## 2.2 particle decays and hadrons

### 2.3 The LHC and LHCb

#### 2.3.1 The LHC

The Large Hadron Collider (LHC)[7] is the most powerfull particle-accelerator on planet earth. With a circumference of 26,7km it is also the longest ring accelerator and it lies between 45m and 170m below the surface near Geneva in Switzerland. The tunnel was constructed for the LEP experiment between 1984 and 1989 and is operated by the European Organization for Nuclear Research (CERN). The LHC can produce centre of mass energies of  $\sqrt{s} = 13$  TeV in proton-proton collisions during Run 2. After the upgrade the LHC will collide particles with the centre of mass energy of around  $\sqrt{s} = 14$  TeV. An image of the accelerators and the experiments is shown in fig. 2.2.

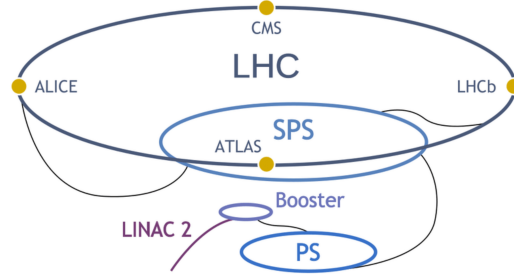


**Abbildung 2.2:** an overview of the LHC facilities[1].

By ionizing hydrogen gas, protons are created and accelerated to 50 MeV by the linear accelerator (LINAC 2). Afterwards the beam is injected into the Proton Synchrotron and the Super Proton Synchrotron to a maximum of 450 GeV before the beam is brought into the LHC. The beam contains several bunches with around  $1,15 \cdot 10^{11}$  protons per bunch and a bunch spacing of 25 ns. The LHC houses four major experiments. ATLAS and CMS are classified as general purpose detectors with a detection range of close to  $4\pi$ . The interaction in these detectors is located in the very center so that tracks going in every direction can possibly be found. Searches for the Higgs Boson is just one of many physics aspects these detectors are built for. The other two Experiments located at the LHC are ALICE and LHCb. The ALICE experiment mainly studies the quark-gluon plasma during the runs with lead ion collisions instead of protons. In this thesis the Scintillating Fibre Tracker (SciFi Tracker) located at the LHCb will be focused on and discussed in the following chapters.

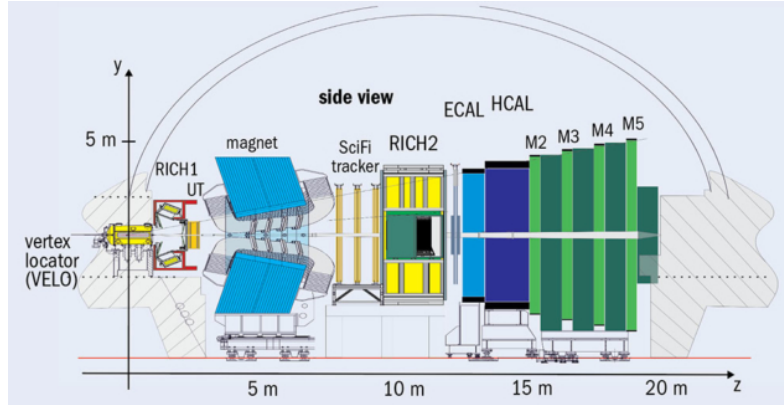


Abbildung 2.3: a sideview of the LHCb experiment[2].

### 2.3.2 The LHCb

For high energies,  $b$ - and  $\bar{b}$ -hadrons are heavily produced in a tight forward direction<sup>2</sup>. The LHCb experiment[13] is a forward spectrometer covering  $2 < \eta < 5$  in the pseudorapidity range. This experiment's main physics goal is beauty quark physics. A sideview of the LHCb is shown in figure 2.3. The LHCb consists of several smaller detector components namely the Vertex Locator (VELO) right on the interaction point, two Ring Imaging Cherenkov counter (RICH 1 and RICH 2), in front of the spectrometers lies the Trigger Tracker and behind them the SciFi Tracker which is the important part of this thesis. Further back a Preshower (PS) is mounted followed by the electromagnetic calorimeter (ECAL) and the hadronic calorimeter (HCAL). In the very back, several muon chambers are mounted for every track that is yet to be determined.

In this section, a general overview about the requirements for the SciFi Tracker as well as the layout will be described based on the presentation in the *technical design report*[8] of the upgrade.

The upstream and downstream trackers provide a good precision estimate of the momentum of charged particles so that mass resolution of decayed particles can be precisely measured. For particle identification the reconstructed trajectories of charged particles are used as input for the RICH detectors. The limiting factor for the momentum resolution is multiple scattering for tracks with a momentum lower than  $80 \frac{\text{GeV}}{c}$ . For tracks with a higher momentum the detector resolution is the limiting factor.

<sup>2</sup>They are also produced in a tight backward direction but the experiment is only built for the forward cone.

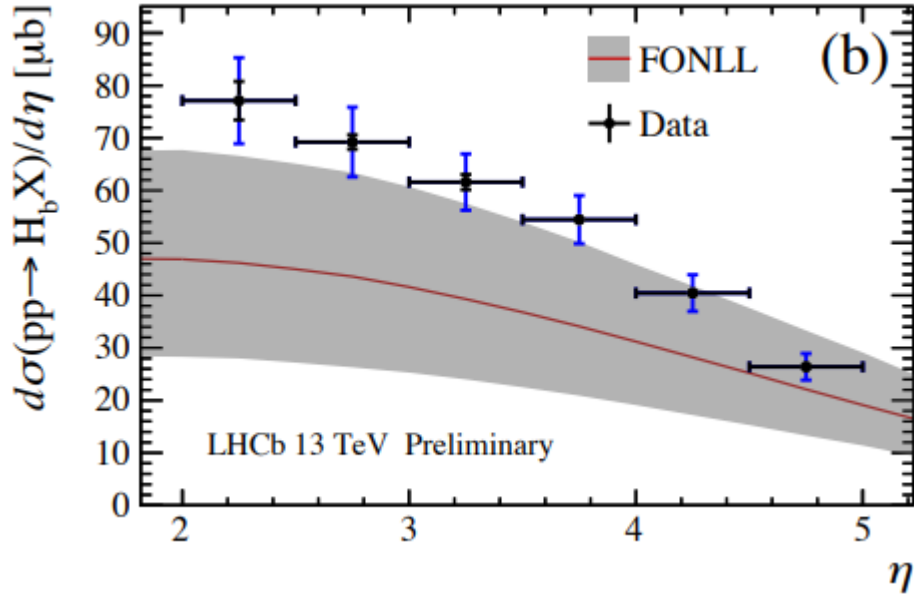


**Abbildung 2.4:** branching ration of  $b$  and  $\bar{b}$  production in forward direction. Shown is the data versus fixed-order plus next-to-leading logs(FONLL)[4][5].

The SciFi Tracker replaced the inner Tracker (IT) and the outer Tracker (OT) and is located in the same place as the downstream trackers that were previously installed.

The instantaneous luminosity after the upgrade is expected to be  $1 \text{ 1}/(\text{cm}^2 \text{ s})$  bis  $2 \cdot 10^{33} \text{ 1}/(\text{cm}^2 \text{ s})$  with a bunch spacing of 25 ns. The average number of proton-proton interactions per bunch crossing will be between  $\nu = 3.8$  and  $\nu = 7.6$ .

### 2.3.3 Layout of the SciFi Tracker

The SciFi Tracker consists of three stations T1, T2 and T3 each having four layers ( $X1, U, V, X2$ ). The orientation of these planes with respect to the vertical axis are  $(0^\circ, 5^\circ, -5^\circ, 0^\circ)$ . Since the beampipe is not exactly parallel to the ground the vertical axis is defined as vertical on the z-axis of the beampipe. The tilted layers are called stereo layers and serve the purpose of 3D hit localization. The layers are 20 mm apart from each other in  $z$ -direction within each station. Each layer has four quarters with each quarter having five<sup>3</sup> modules. Each module is constructed from four fibre mats. A frontal view of the SciFi Tracker is displayed in figure 2.5. The

<sup>3</sup>six for the last (T-)station.

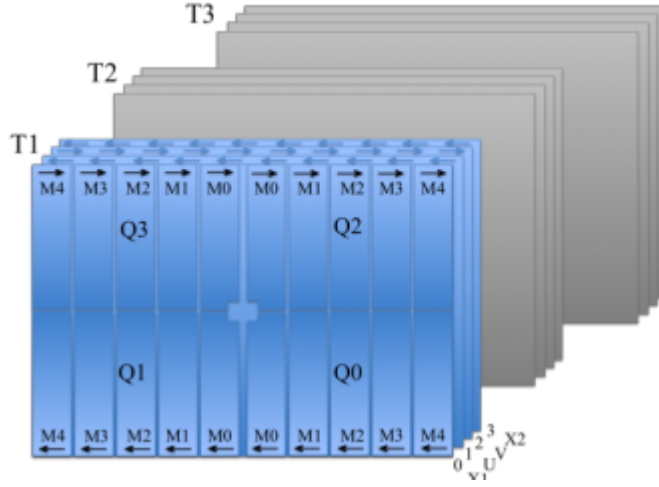


**Abbildung 2.5:** frontal view of the SciFi geometry and readout order[6].

global coordinate system used is of right-handed nature with positive  $z$  pointing away from the interaction point following the beam direction as seen in figure 2.3. positive  $y$  points upwards, towards the surface and positive  $x$  and negative  $x$  are named as A-Side and C-Side respectively[8]. For readout purposes the top and bottom half of each element have inverted  $x$ - and  $y$ -axis as seen in figure 2.5.

To ensure an optimal alignment, a well known geometry is key. Therefore, the fibres must be aligned within  $50\text{ }\mu\text{m}$  bis  $100\text{ }\mu\text{m}$  in  $x$ -direction and must not be more than  $300\text{ }\mu\text{m}$  bent in  $z$ -direction.

### 2.3.4 Scintillating Fibres

The scintillating fibre material is a polymer with an organic fluorescent dye added to the polystyrene structure to enhance the yield during the scintillation process. In order to produce and register a photon signal, the ionization energy is deposited in the fibre core firstly. The amount of energy need for the polymer to reach an excited state is just a few electronvolts. The added dye has the particular structure to match the excitation energy. The dye generates excited energy states when particles hit the fibre and deposit their energy. The long fibre mats and the refractive index make sure total reflection on the inside happens which guides the photons to the SiPMs<sup>4</sup>. On the opposite end of the SiPM a full reflective mirror is mounted so the photons travelling to the other end do not get lost but reflected towards the SiPM.

<sup>4</sup>Silicon Photomultiplier

## 3 The Theory of Alignment

short introduction

### 3.1 Track Reconstruction

In order for LHCb to be used for physics, all of the detector hit information has to be converted into tracks, which is a challenging task. The track reconstruction algorithm needs to find the correct hits from each subdetector to build the track. This can be problematic just because of the amount of tracks per events (roughly 100). It is crucial to find all particle tracks and also their track parameters which come from the track fit.

A good track fit is needed in order to find the best estimates for the track parameters and covariances. The estimates are used in the event reconstruction to find the correct tracks for each particle and the decay products. The info provided is used in the RICH rings, ECAL and HCAL and muon detectors. With these information, particle and track parameters such as the invariant mass can be measured and vertex origins can be found. There are several track models that can be used. In general, a track is build from numerous segments which are either straight or curved because of an active magnetic field. Depending on the environment of the track either model is good. The track segments are called track states and are defined by a position in  $x$  and  $y$  at a given distance  $z$  where the hit was located, then a tangent direction  $t_{x,y}$  at the hit position and a momentum parameter acquired from the track curve inside the magnetic field[15].

In order to correctly reconstruct the track it is important to know where the hit is localized and for the upcoming hits, where the particle track came from. From the momentum measurement of the track curvature caused by the magnetic field, the parameter  $q/p$  is also added.



$$\vec{r} = \begin{pmatrix} x \\ y \\ t_x \\ t_y \\ \frac{q}{p} \end{pmatrix} \quad t_x = \frac{\partial x}{\partial z} \quad t_y = \frac{\partial y}{\partial z}$$

The uncertainty of the five-component state vector is a  $5 \times 5$  covariance matrix  $C$ . A track state can be anywhere on the trajectory but is easier to choose it at real detection points. Combining the track state with a real measurement point is called *node*. The propagation from node  $k - 1$  to node  $k$  is described by a propagation function

$$\vec{r}_k = f_k(\vec{r}_{k-1}) + \vec{w}_k.$$

This means node  $k$  is acquired by propagating node  $k - 1$  through the propagation function  $f_k$  and shifting it by the *process noise*  $\vec{w}_k$ . LHCb uses process noise to model the scattering. Depending on the type of propagation, linear or curved, a different propagation function is used. for a linear extrapolation,  $f_k$  results in

$$f_k(\vec{r}_{k-1}) = F_k \vec{r}_{k-1}$$

with the transport matrix  $F_k$

$$F_K = \begin{pmatrix} 1 & 0 & \Delta z & 0 & 0 \\ 0 & 1 & 0 & \Delta z & 0 \\ 0 & 0 & 1 & 0 & 0 \\ 0 & 0 & 0 & 1 & 0 \\ 0 & 0 & 0 & 0 & 1 \end{pmatrix}$$

and  $\Delta z$  being the difference in  $z$  between the nodes

$$\Delta z = z_k - z_{k-1}$$

Trajectory information for each node is provided by the real measurement where the relation between measurement  $m_k$  and track state at a given node  $k$  is defined as

$$m_k = h_k(\vec{r}_k) + \epsilon_k$$

with the projection function  $h_k$  and *measurement noise*  $\epsilon_k$ . So if the detector only measures the  $y$  coordinate of state, the projection function will be

$$h_k(\vec{r}_k) = H_k \vec{r}_k$$

with

$$H_k = \begin{pmatrix} 0 & 1 & 0 & 0 & 0 \end{pmatrix}$$

When measuring more parameters the measurement matrix  $H_k$  and projection matrix have dimension  $n \times 5$  with  $n$  being the numbers of parameters measured.

With this track model,  $\epsilon_k$  and  $w_k$  are random and unknown and have an expectation value of zero.

## 3.2 The Kalman filter method [15]

In general a track is an ensemble of measurements and track states and the Kalman filter method is used to fit tracks. The idea of the Kalman filter is, to have a starting node and add measurements one by one. In between the addition of measurements, the local track state is updated with the new information. The Kalman filter method is a  $\chi^2$  minimising problem for the measurement of the track. Because of the iterative nature of the method, it is fast und also used in other fields than physics, for example GPS and meteorology. The three steps of the Kalman filter will be briefly outlined and later discribed in further detail.

The first step is the **Prediction**: The next track state of the trajectory is predicted based on the track state at the previous node. The second step is the **Filter** procedure: By using filter equation\*s, the prediction is updated with measurement information in this node. The prediction and filter are repeated for each measurement. With more measurements added, the estimate for the best trajectory is the track state after each filter step. The final step is called **Smoother**: When the trajectory is complete, smoother equation\*s are applied from the last node to the previous node. Therefore the information from all measurements is used in both forward- and backpropagation which results in a more defined track.

### 3.2.1 first Step: Prediction

For a given state vector at node  $k-1$ , the prediction for the  $k^{\text{th}}$  state vector and its covariance matrix results from the propagation relations

$$\begin{aligned}\vec{r}_p^{k-1} &= f_p(\vec{r}_{k-1}) \\ \text{Cov}_k^{k-1} &= F_k C_{k-1} F_k^T + Q_k\end{aligned}$$

The superscript of the statevector shows the amount of information used in the estimate. That means  $\vec{r}_k^n$  is the smoothed state vector which used all information,  $\vec{r}_k^{k-1}$  is the predicted state vector and  $\vec{r}_k^k \equiv \vec{r}_k$  is the filtered state.

$Q_k$  is the process noise in matrix form and it is part of the predicted covariance matrix  $C_k^{k-1}$ . Because the first state cannot take measurements from the previous state, an initial prediction is taken from the track finding algorithm instead. The predicted residual between the measurement,  $m_k$  and the state vector results in

$$\text{res}_k^{k-1} = m_k - h_k(\vec{r}_k^{k-1})$$

and the corresponding covariance matrix is defined as

$$\text{Cov}_{\text{res},k}^{k-1} = V_k + H_k C_k^{k-1} H_k^T.$$

Here,  $V_k$  is the measurement variance. With these metrics the minimal  $\chi^2$  for the optimal track states can be calculated via

$$(\chi^2)_k^{k-1} = \text{res}_k^{k-1} (\text{Cov}_{\text{res},k}^{k-1})^{-1} \text{res}_k^{k-1}$$

### 3.2.2 second Step: Filter

During the filter step, the track state is updated with the measurement information. Iteratively, each measurement is added and the filtered state  $\vec{r}_k$  and the corresponding covariance matrix is calculated via

$$\begin{aligned}\vec{r}_k &= \vec{r}_k^{k-1} + G_p \text{res} + k^{k-1} \\ \text{Cov}_k &= (\mathbb{1} - G_k H_k) \text{Cov}_k^{k-1},\end{aligned}$$

where  $G_k$  is the gain matrix of dimension  $5 \times 1$  and is defined as

$$G_k = C_k^{k-1} H_k^T (\text{Cov}_{\text{res},k}^{k-1})^{-1}$$

Afterwards the residuals and its covariance matrix are calculated and the filtered total  $\chi^2$  is defined as

$$(\chi_{\text{filter}}^2)_k = \text{res}_k \text{Cov}_{\text{res},k}^{-1} \text{res}_k .$$

The prediction and filter procedure is continued for all measurements until the track is fully reconstructed. Because the last node at  $k = n$  has the most information in it, a backward update is performed to infuse the previous nodes with the same information as in last node. This is called *smoother*-step.

#### 3.2.3 third Step: Smoother

The smoother function returns the best possible estimate for track states at the previous nodes. The method used is called *Rauch-Tung-Striebel*-smoother[12]. The idea is to use backward information and construct a smoothed state vector and covariance matrix

$$\begin{aligned} \tilde{r}_k^n &= \vec{r}_k + S_k (\vec{r}_{k+1}^n - \vec{r}_{k+1}^k) \\ \tilde{C}_k^n &= C_k \end{aligned}$$

and the Smoother-matrix  $S_k$  of dimension  $5 \times 5$

$$S_k = C_k F_{k+1}^T (C_{k+1}^p)^{-1} .$$

In order to calculate the smoothed  $\chi^2$  the residual and corresponding covariance matrix are

$$\begin{aligned} \text{res}_k &= m_k - h_k \vec{h}_k^n \\ \text{Cov}_{\text{res},k}^n &= V_k - H_k C_k^n H_k^T \end{aligned}$$

The  $\chi^2$  is calculated analogously to the one during the filter step with the difference being the new residuals and covariances.

### 3.3 alignment using derivatives

this will come later. time ran out last week so this will be done later.

## 4 Alignment of the SciFi

The alignment is performed using run2 data as well as Monte Carlo samples. The goal is to find the optimal configuration for the SciFi to mirror the real detector. A configuration is defined as a set of constraints, degrees of freedoms and alignable objects such as the stations, layers, halflayers, modules or fibre mats. The following pre-installed alignment conditions with the survey constraints are used.

```

FT : 0 0 0 0 0 0 : 1 1 1 0.0003 0.0003 0.0003
FT/T. : 0 0 0 0 0 0 : 1 1 1 0.0003 0.0003 0.0003
FT/T./ Layer (X1|U|V|X2) : 0 0 0 0 0 0 : 0.2 0.2 0.2 0.0001 0.0001 0.0001
FT/.*Module. : 0 0 0 0 0 0 : 0.1 0.1 0.1 0.001 0.001 0.001
FT/.*Mat. : 0 0 0 0 0 0 : 0.05 0.05 0.05 0.1 0.1 0.1

```

The string is the name of the element, the first set of six numbers are hardcoded parameters for each of the 3 translation degrees of freedom and 3 rotational degrees of freedom (Tx, Ty, Tz, Rx, Ry, Rz) and the second set of six parameters are the corresponding uncertainties.

The scale for the translations are mm and the scale for the rotations being rad. A survey uncertainty of 0,0001 stands for 0,1 mrad.

The alignment runs were performed with alignment specific packages from Alignment/Escher and Alignment/TAlignment[3].

During the alignment, lagrange constraints can be utilized to minimize alignment parameter  $\alpha$  under the condition

$$f(\alpha) = 0 \quad (4.1)$$

and adding the lagrange parameter  $\lambda$  to get

$$\Delta\chi^2 = \lambda f(\alpha). \quad (4.2)$$

Lagrange constraints are added to fix loosely constrained degrees of freedom and can be used for any linear combination of translations and rotations.

## 4.1 Nulltests and software tests

As a starting point, the Alignment version v17r1 was used with 5000 events, magnet in upward position and *GoodLongTracks*. The *GoodLongTracks* have the following cuts and parameters:

- $P_{\text{total, min}} = 5000 \text{ MeV}$
- $P_{\text{total, max}} = 200\,000 \text{ MeV}$
- $p_{T, \text{min}} = 200 \text{ MeV}$
- maximum  $\chi^2 = 5$
- track type should be categorized as "long"

and for the later used *HighMomentumTTracks* the cuts and parameters are:

- $P_{\text{total, min}} = 50\,000 \text{ MeV}$
- track type should be categorized as "TTrack"
- maximum  $\chi^2 = 5$

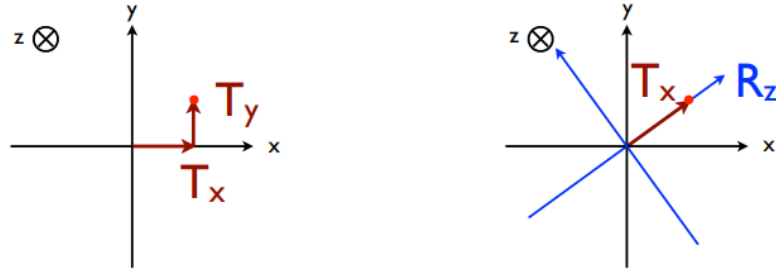


**Abbildung 4.1:** Different ways of describing a measurement point inside the detector (quelle gibt es nicht mehr -> selber zeichnen oder anderes bild).

At first, a series of tests regarding different degrees of freedom and lagrange constraints is performed to find the optimal solution for the SciFi.

The real detector layers are all centered around the beam pipe with no shifting in any direction and the goal is to align the layers in the software to mirror the real layers and reduce the shifting as close to zero as possible.

Figure 4.1 is used to demonstrate which degrees of freedom can be used to describe a point in the detector or a shift in coordinates. On the left-hand side the measurement point is described through cartesian coordinates and on the right-hand side it is described via polarcoordinates in a way.

The starting point of the analysis was the presentation held by Florian Reiss[10] which contained findings about malfunctioning shearing constraints. His analysis was performed with the VELO but the ideas are applicable for the SciFi as well. The parameters he used were changed to fit the SciFi and resulted in

```
dofs = "TxTyRxRy"
elements.FTStations(dofs)
elements.FTFrameLayers(dofs)
TrackSelections = GoodLongTracks()
```

The alignable objects are the (T-)stations and te layers and the trackselection is chosen to be *GoodLongTracks* as a starting point. This will be called *baseline*<sup>1</sup>. The baseline is unconstrained in order to see what the software geometry of the detector is like before the alignment with constraints.

In this part, the steps of testing different configurations is described and analysed.

Starting of with the first configuration called "noRotation" tested against the baseline as seen in figure 4.2 for 1000 simulated events used in this particular alignment run and 4.3 for 7000 simulated events respectivley.

The measurement points are the mean of each layer, the errorbars are root-mean-square errors (RMS) and come from the difference between the C-side and the A-side of the detector layer and is not the measurement uncertainty.

The "noRotation" configuration is defined as:

```
dofs = "TxTz"
elements.FTStations(dofs)
elements.FTFrameLayers(dofs)
TrackSelections = GoodLongTracks()
constraints = [
    "station1_:_FT/T1_:_Tx_:_Tz",
    "station2_:_FT/T2_:_Tx_:_Tz",
    "station3_:_FT/T3_:_Tx_:_Tz",
    "frontCSide_:_FT/T3/Layer(X1|U)/Quarter(0|2)_:_Tx_:_Tz",
    "backCSide_:_FT/T3/Layer(V|X2)/Quarter(0|2)_:_Tx_:_Tz",
    "frontASide_:_FT/T3/Layer(X1|U)/Quarter(1|3)_:_Tx_:_Tz",
    "backASide_:_FT/T3/Layer(V|X2)/Quarter(1|3)_:_Tx_:_Tz"
]
```

---

<sup>1</sup>or baseline configuration

Here, only x-translation will be compared since other translatory degrees of freedom will be swapped out for a rotational degree of freedom. The first three constraints on all stations regarding translations brings the total movement of the station to around zero which can be seen clearly in figure 4.2. The last four constraints restrict the movement of each side of the C-frame to be centered around zero which brings the x translation in station 3 even closer to zero. Even though the alignment improved the amount of constraints cannot recover from potential misalignments because the constraints hinder the stations from moving.

Later on we want as few constraints as possible so that the alignable objects can be aligned and converge towards the optimal position based on the track reconstruction. This measurement only used 1000 events and is only used as a guideline to what the trend of the distribution looks like. The associated graphs for  $T_x$  plotted against the group position in  $z$  are shown in figure 4.2. A prominent problem visible is the layer separation between the X-layers and the stereo layers as well as a separation between the C-frames inside each station.

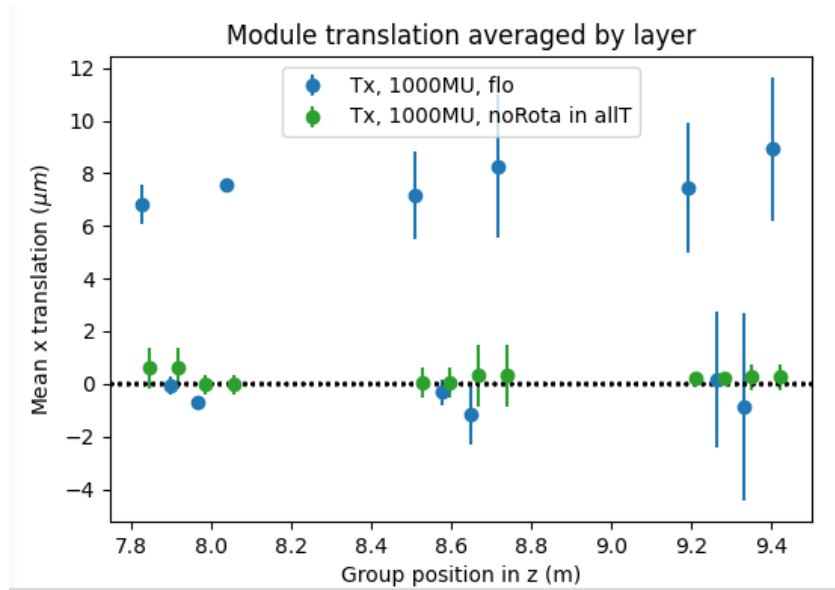


**Abbildung 4.2:** comparison of different configurations without rotational constraints in every station, magnet up and 1000 events. plotted is translation in x versus global z.

In figure 4.3 the same measurement was performed for 7000 events to get a better picture. In comparison to 4.2 an overall improvement of the baseline is visible and the layer-splitting is reduced but still prominent. The green measurement shows no direct improvement since the layers are already pretty close to zero in x-direction.



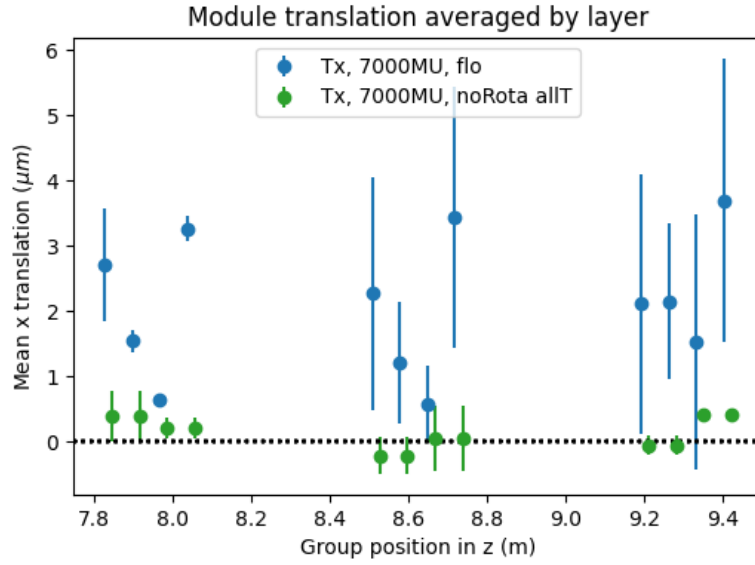


**Abbildung 4.3:** comparison of different configurations without rotational constraints in all stations, magnet up and 7000 events. plotted is x translation versus global z.

Using 7000 events instead of 1000 events showed a more realistic picture but took more time to compute especially for 10 alignment iterations. For the following configuration, 3000 simulated events were used to shorten the computing time while still yielding an accurate representation of the situation.

The next configuration tested will be called "half C-frame". This configuration is defined as

```
dofs = "TxTzRxRz"
elements.FTStations(dofs)
elements.FTFrameLayers(dofs)
TrackSelections = GoodLongTracks()
constraints = [
    "station1_::FT/T1_::Tx_Tz",
    "station2_::FT/T2_::Tx_Tz",
    "station3_::FT/T3_::Tx_Tz",
    "frontCSide_::FT/T3/Layer(X|U)/Quarter(0|2)_::Tx_Tz::total",
    "backCSide_::FT/T3/Layer(V|X2)/Quarter(0|2)_::Tx_Tz::total"
]
```

and the comparison to the baseline is shown in figure 4.4. Here the stations and layers

are aligned in  $Tx$ ,  $Tz$ ,  $Rx$  and  $Rz$  but the stations are still only constrained in their translations. Also, the last station only has one side of each C-frame constrained. The additional keyword **total** constraints the difference of the quarters to zero with respect to the nominal position. As seen in figure 4.4 the first two layers have an average position of zero but the individual position is not. The same is seen in the last two layers of each station.

This new configuration in orange converged after 15 iterations. Normally, an alignment job should converge after three to five iterations. If the convergence happens later there could be a problem with the constraints which prevent the alignment from converging because they are implemented wrongly, are redundant or weak modes hinder the convergence.

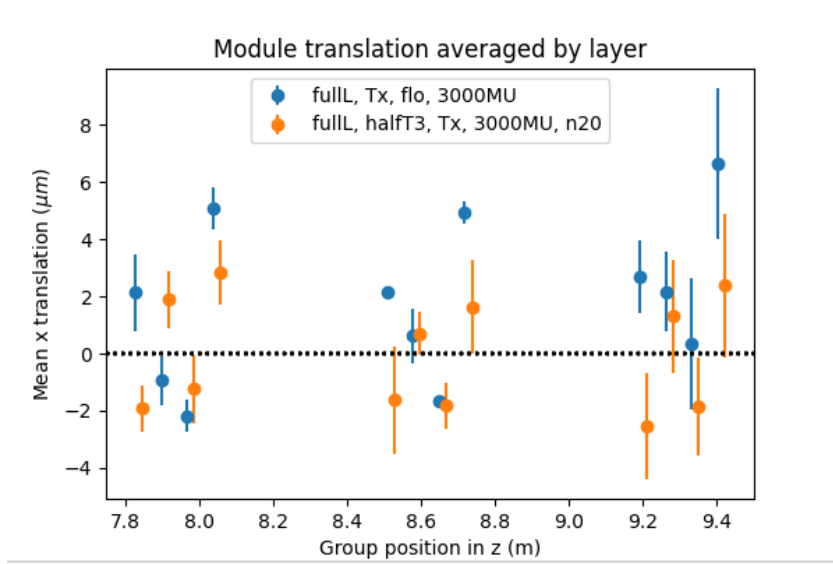


**Abbildung 4.4:** analysed 20 iterations for x translation behavior (look up exact constraints and dofs)

The consequences of very strict  $Tx$  constraints are shown in figure 4.5. The difference between the configuration used here and the one used in figure 4.3 are... (comparison todo).

Introducing halflayers as an alignable, they are constrained in station 3 because we found that it results in the best alignment. Also halflayers are a better representation of the real detector since we describe the C-side and A-side separately. This is due to the fact that station 3 is the furthest away from the interaction point (IP) and  $q/p$  has the most impact at that distance. Looking at  $Tz$  first, the RMS uncertainty is viewed by looking at the A-side and the C-side separately. A clear layer separation

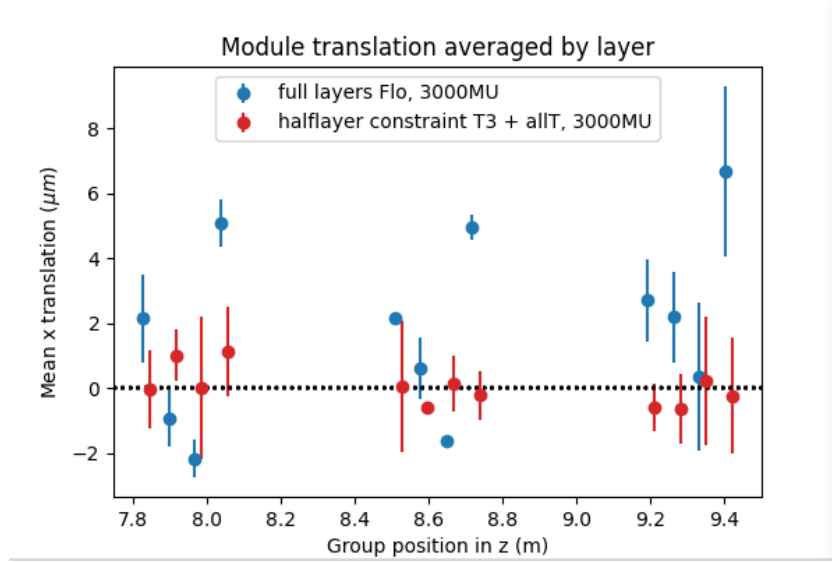


**Abbildung 4.5:** halflayer constraints and full layer constraint, very strict (look up exact constraints and dofs)

is visible in terms of layer translation along the beam pipe 4.6. The first and third layer in each station move away from the IP and the second and fourth layer move away from the IP. Because of the many constraints that are applied to T3, the RMS uncertainty in the other stations gets worse. Because the last station is overconstrained the track reconstruction moves the other stations accordingly which results in larger RMS uncertainty in station 1 and 2.

On the other hand the x-translation 4.7

Looking at figure 4.7, the last two layers in station 3 are separated from the first two regarding x-translation. Especially the last station should be fixed around zero with the constraints added. The sum of all translations should be zero with each individual layer movement being small.

The result is unexpected with the constraints added and the cause of this problem is described later.

#### 4.1.1 rotational constraints

The impact of rotational constraints is looked at in the following chapter. Firstly, comparing the baseline versus a new configuration with added constraints. The direct

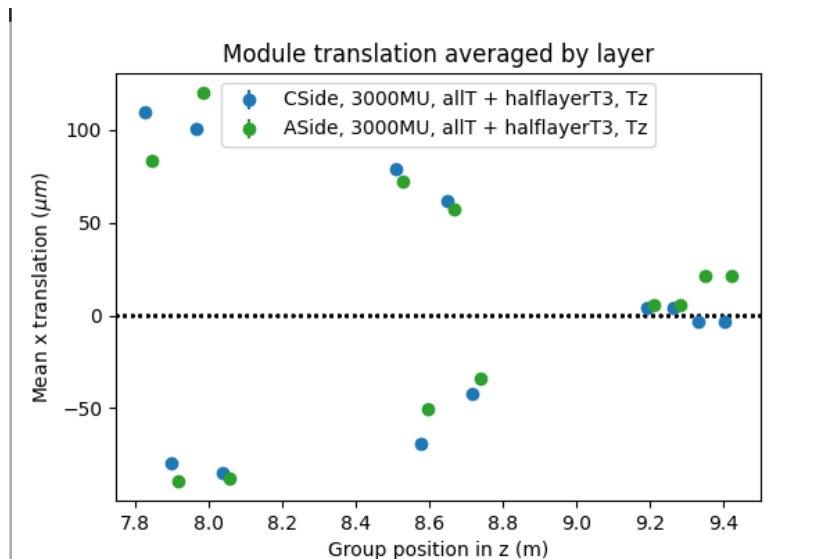


**Abbildung 4.6:** compare C-Side to A-Side for translation in z direction. (look up exact constraints and dofs)

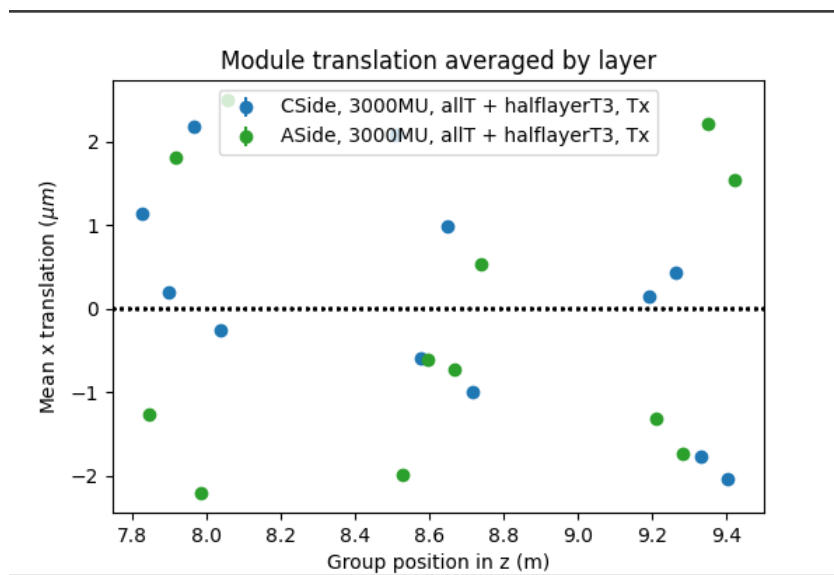


**Abbildung 4.7:** compare C-Side to A-Side for translation in x direction. (look up exact constraints and dofs)

impact to the rotations are quite small but the translations in z- and x-direction show a small improvement to the previous configuration seen in figure 4.5.

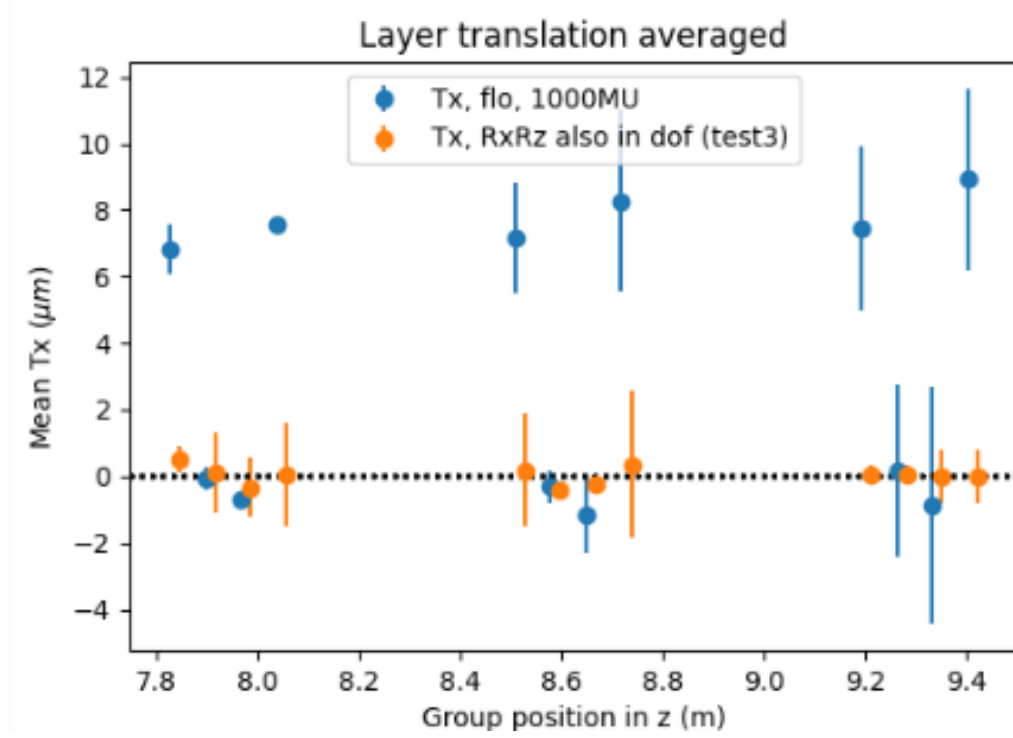


Abbildung 4.8: Tx versus global z.

Now, we have a configuration<sup>2</sup> which is quite ok but has a lot more room for improvement but is nevertheless a better representation than the baseline. Therefore we will now compare further configuration drafts to the "config5" with the following constraints

- constraint 1
- constraint 2
- constraint 3
- ...

and the dataset used is taken from the bookkeeping (which exact one).

In figure 4.9 config5 is plotted against itself but with and added constraint to Rz. The change is the constraint: (fill constraint here). Regarding the goal to reduce the

<sup>2</sup>The always used configuration will be always called "config5" in the labels

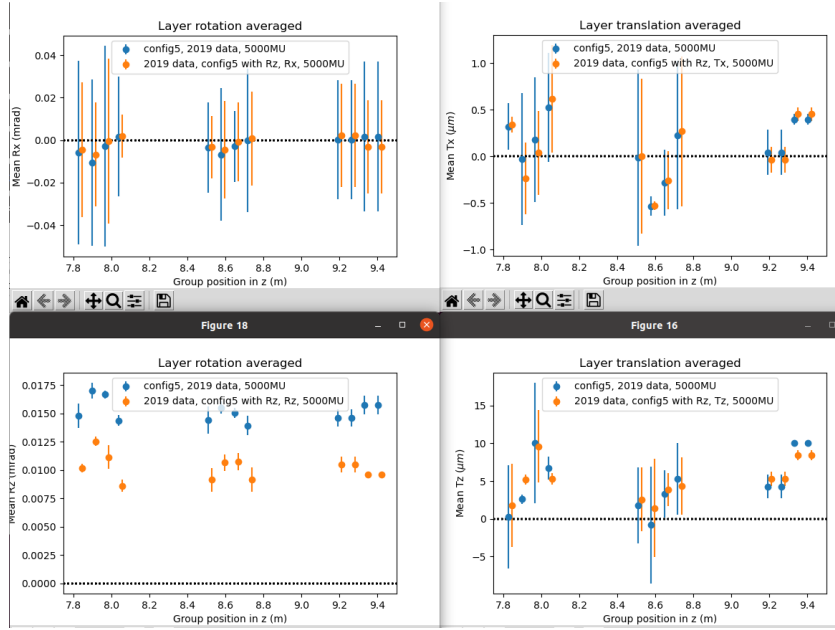


**Abbildung 4.9:** config5 versus config 5 with Rz constraint for rotational improvement.

amount of rotation and translation in each station, the result is a small improvement in  $Rz$  of around 0,005 mrad in every layer.  $Rx$  is mostly unchanged as well as  $Tx$ . The rotation around  $z$  is correlated to the  $z$  translation therefore we see small changes in every layer as well. It is noteworthy, that both X-layers in T2 in the x-translation plot have a quite large RMS uncertainty which means the A-side and the C-side in the X-layers are quite far apart but the mean is right around 0. That is expected since the constraint added only brings the mean of the layer to 0. In future analyses another constraint should be added to also keep the side themselves small.

In comparison to what florians configuration looks like against the new proposed configuration the figure 4.10 can be looked at. The alignment was performed for 10 iterations and the alignable degrees of freedom are  $Tx$ ,  $Tz$ ,  $Rx$ ,  $Rz$ . The alignable elements are the stations and the framelayers. The constraints used are:

```
station3 : FT/T3 : Tx Rz Rx Rz
backCframeT3 : FT/T3/Layer(V|X2) : Tx Tz
FT/T3X1UCSide : FT/T3/Layer(X1|U)/Quarter(0|2) : Tx Tz Rx Rz
FT/T3VX2CSide : FT/T3/Layer(V|X2)/Quarter(0|2) : Tx Tz Rx Rz
FT/T3X1UASide : FT/T3/Layer(X1|U)/Quarter(1|3) : Tx Tz Rx Rz
```

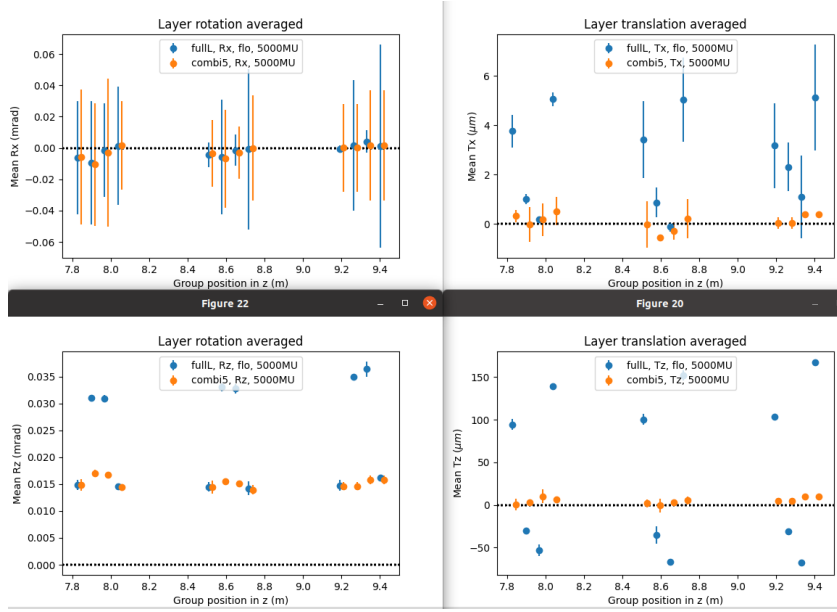


Abbildung 4.10: flo with full layer constraint versus config 5

FT/T3VX2ASide : FT/T3/Layer(V|X2)/Quarter(1|3) : Tx Tz Rx Rz

The first constraint restricts the overall station 3 movement in Tx, Tz, Rx and Rz. The second constraint restricts the total movement of the last C-frame to be 0 but the individual movement can differ. The last four constraints are C-frame constraints as well but for each half layer in station 3.

It is good to see that the layer separation in  $Rz$  is mostly fixed. But there is still an offset from 0 that is troublesome. This will most certainly have something to do with the clusterbias. Regarding Tx, we have managed to bring down the x-translation to roughly 0 which is a good improvement for the null tests of Tx.

Translation constraints as well as rotation constraints are not the only constraints tested. There are also scaling- and shearing constraints that were analysed but seemed to have no major impact.

## 4 Alignment of the SciFi

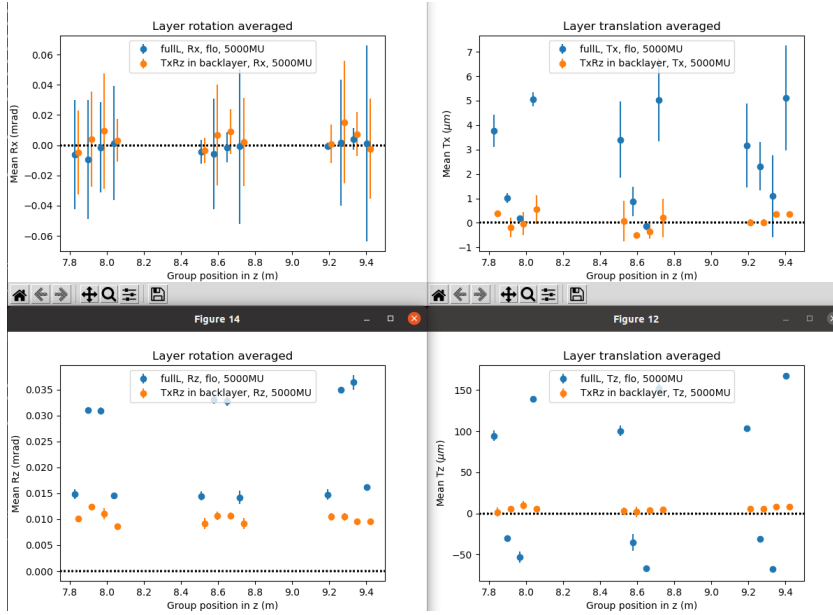


Abbildung 4.11: dofs Tx Rz and backlayer constraints.

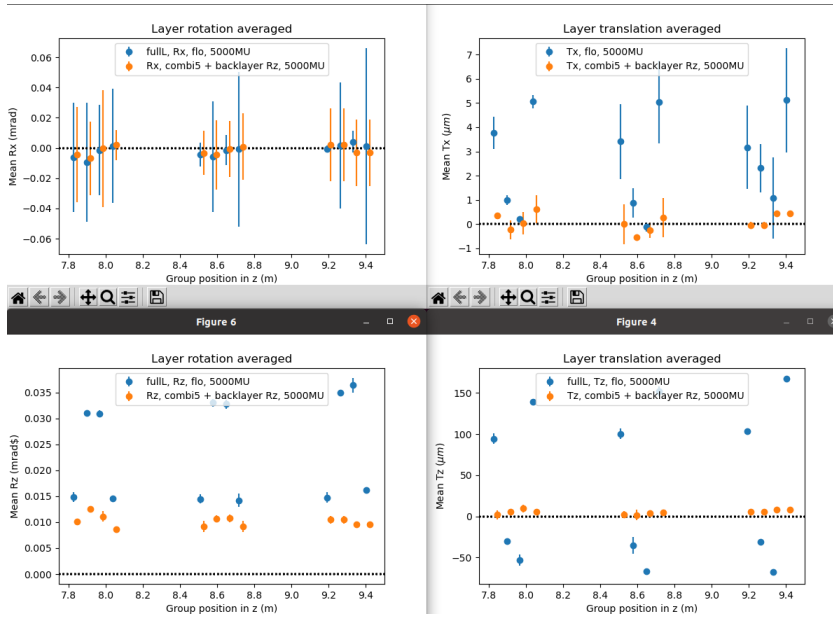


Abbildung 4.12: combi 5 with Rz backlayer constraint.



## 4.2 $\chi^2$ tests and weak modes

In this section, a  $\chi^2$  analysis is performed in order to study the "goodness" of the alignment since the better the  $\chi^2$  after the alignment the better. The second aspect i want to cover is the impact of potential weak modes also known as "correlated alignment parameters". There are several weak modes that could occur namely *global translation*, *shearing* and *curvature bias*. Weak modes are unaffected by the  $\chi^2$  since the residuals do not change but they do however show inside the eigenvalues of track parameters. The effect weak modes have on the alignment are biases regarding track parameters and late convergences. There are different solutions that can be utilized to reduce the effect from weakmodes such as

- using other configurations like magnet off or mass plots for off-axis events
- utilizing other survey data sets
- using kinematic and vertex constraints

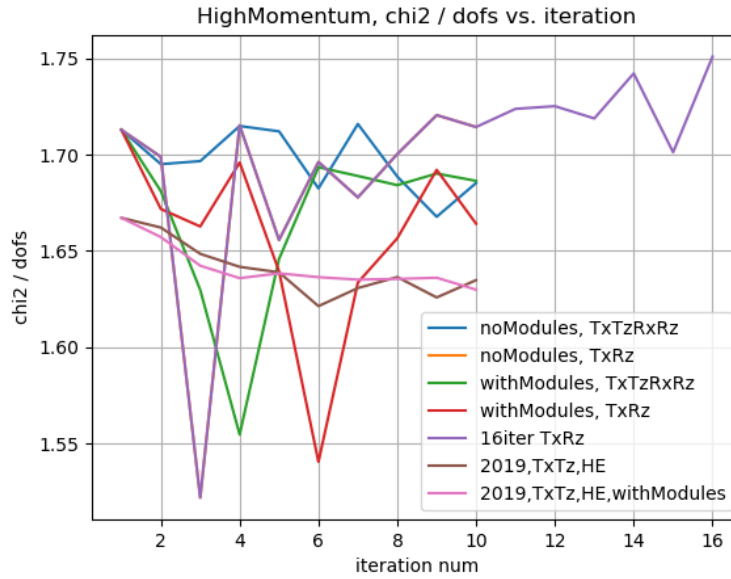


**Abbildung 4.13:**  $\chi^2/dofs$  versus iteration number of different degrees of freedom, alignables and data samples.

We started with the  $\chi^2$ -analysis for *HighMomentumTTracks*, 6500 events and 2020 data plotted versus the iteration number during the alignment in figure 4.13. In blue,

stations and layers were aligned in  $Tx$ ,  $Tz$ ,  $Rx$  and  $Rz$  with the constraints being used from "config5". The orange measurement is identical except for the degrees of freedoms being only  $Tx$  and  $Rz$ . In green and red the same measurements as in blue and orange were performed with the difference that that the modules are aligned as well. The purple measurement is the only one which covers 16 iterations and is otherwise identical to the orange one. That is also why the orange measurement is not visible since it lies behind the purple one for the first 10 iterations. the brown and pink measurements are done for 2019 data and are otherwise identical to the orange and red measurement regarding constraints and alignable degrees of freedom.

The spikey behavior is not what we expected and this might be the result of weak modes since the convergence is quite bad in all of the 2020 data which can be seen by the not steadily decreasing  $\chi^2/dofs$ . The 2019 measurements were performed as control measurements with and without module alignment. Here a clear decrease in the  $\chi^2/dofs$  is visible. This indicates that for the 2020 data additional analysis must be performed to gain further knowledge about the dataset since it shows some unclear findings.

The idea to test  $Tx$ ,  $Tz$ ,  $Rx$  and  $Rz$  versus only one translation and one rotational degree of freedom was to analyse the effect regarding the convergence and the  $\chi^2/dofs$  itself. One could also argue that there was a quick convergence after three iterations when looking at the yellow measurement but something happened afterwards. This will be analysed in a future project.

Also, in figure 4.14 the same plot is presented but only for the first four measurements clean up the image. The same four  $\chi^2$  measurements were plotted against the number of tracks as seen in figure 4.15. It is pleasing to see a steady decrease in  $\chi^2/dofs$  with an increasing number of tracks. This was done as a consistency check.

In figure 4.16 a side-by-side view of the same  $\chi^2$  measurement is shown but for different number of events. Despite the different labels these are the same measurements, only the colors are switched around for red and green and also yellow and blue as a pair. The thing that strikes the eye is the steadily decrease in  $\chi^2/dofs$  in the red measurement. Unlike our first expectations that  $Tx$  and  $Rz$  are enough degrees of freedom to describe the system using additional degrees of freedom seemed to help the alignment. Also, the blue measurement sits behind the orange which might be due to an programming error.

In figure 4.17 a consistency check for figure 4.16 was performed. The number of tracks correlate good with the  $\chi^2/dofs$ . The blue measurement is missing again which seems to be a programming error.

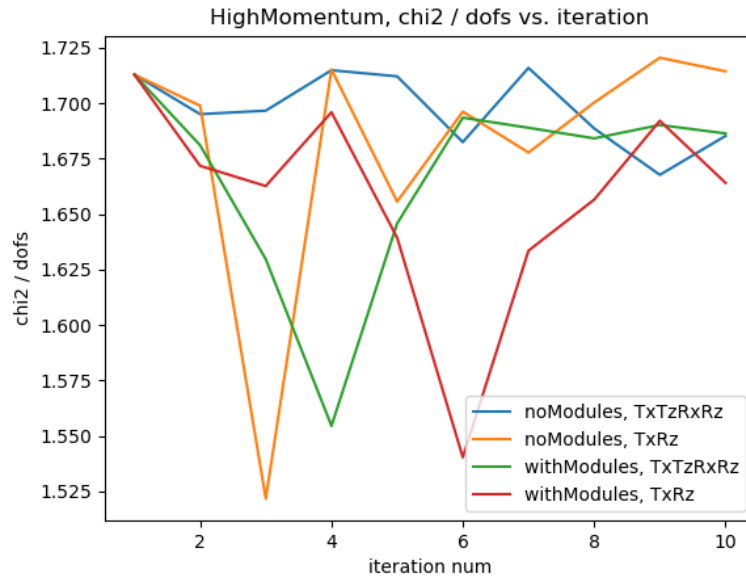


**Abbildung 4.14:**  $\chi^2$ -test versus iteration number of different degrees of freedom, alignables and data samples but fewer (redo with grid).

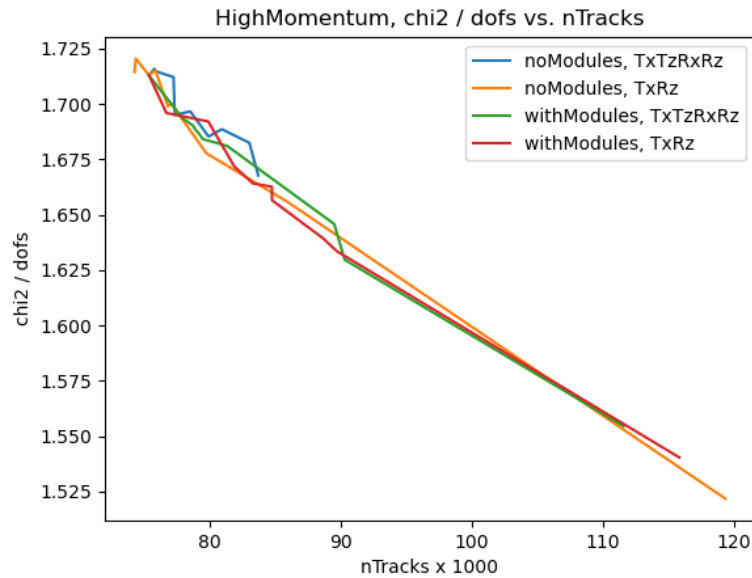


**Abbildung 4.15:**  $\chi^2$ -test versus number of tracks of different degrees of freedom, alignables and data samples but fewer (redo with grid).

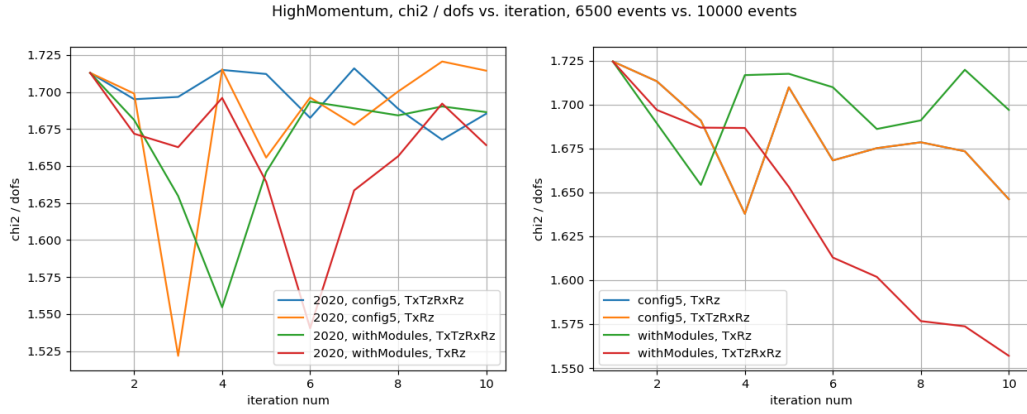


Abbildung 4.16:  $\chi^2 / \text{dofs}$  versus iteration number for different number of events.

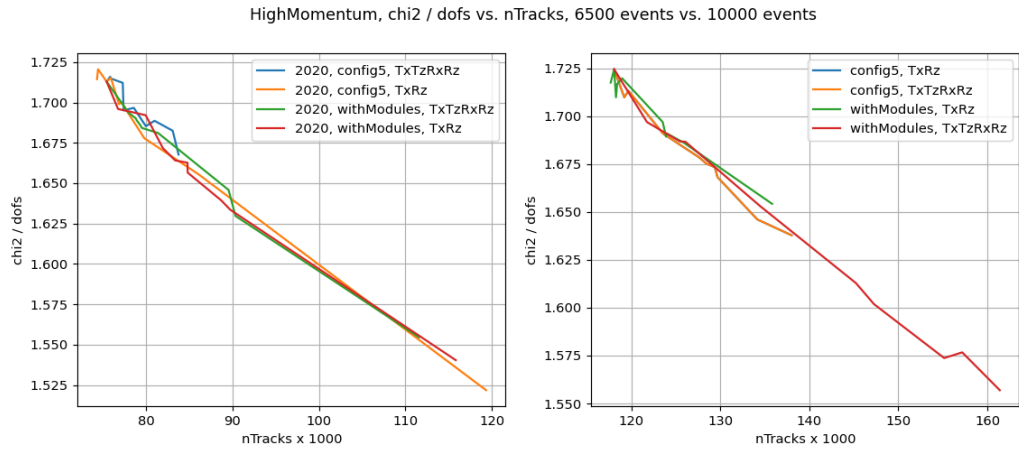


Abbildung 4.17:  $\chi^2 / \text{dofs}$  versus number of Tracks for 6500 events and 10000 events.

### 4.3 luminosity samples and chi2

For a cross check regarding upcoming studies the difference in  $\chi^2/dofs$  for samples of different luminosities are looked at. Comparing two samples, one with a "ramp-up" luminosity with a parameter  $\nu = 3.8$  also referred to as "low luminosity" and one for the luminosity used during the data taking with  $\nu = 7.6$ , called "normal luminosity". Plotted are these samples in  $\chi^2/dofs$  versus the iteration number 4.18 and the number of tracks 4.19.

in figure 4.18 we see the expected convergence after iteration three and a quite low  $\chi^2/dofs$  of around 1,285 95 for the normal luminosity sample and 1,3067 for the low luminosity sample.

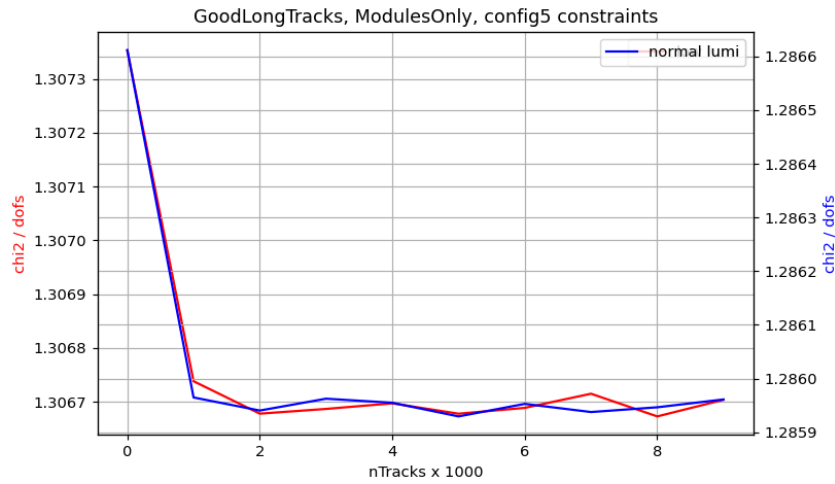
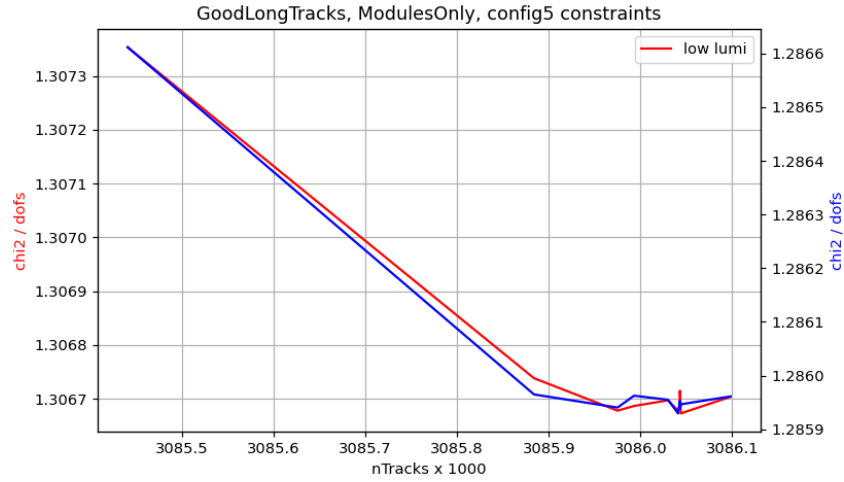


Abbildung 4.18: compare different luminosities and plot  $\chi^2$  versus iteration.



**Abbildung 4.19:** compare different luminosities and plot chi2 versus number of tracks as a measurement for weakmodes and alignment.

## 4.4 impact of the cluster bias

As mentioned earlier the clusterbias most certainly causes the shift in the rotation around  $z$  for each layer so it does not reach 0. To test that a momentary fix was found and implemented. The workaround was to add a scaling to the value ... (look up in LXPLUS) by 0,95.

Figure 4.20 shows the impact of the cluster bias hack regarding the rotation around  $z$ .

As we expected, the amount of rotation was reduced to about 0,004 mrad from the previous 0,01 mrad which is more than a factor of 2 improvement. We also know, that the fix for the cluster bias will not be the only source for the shift and we need further analysis to find the other sources.

Now that we know that the cluster bias can be taken care of we take a closer look at samples of different luminosities since the LHC will not be operated at the maximum luminosity from the start, there is also the ramp up phase where the luminosity will be lower.

Since we want to know what the shifts in rotation and translation will look like when the cluster bias is fixed we will keep it active for the next studies. Figure 4.21 shows the difference between a sample with ramp-up luminosity and a sample with the luminosity during the measurement phase. We see, that the layer separation is much more prominent in station 1 and 3 for the higher luminosity sample but slightly

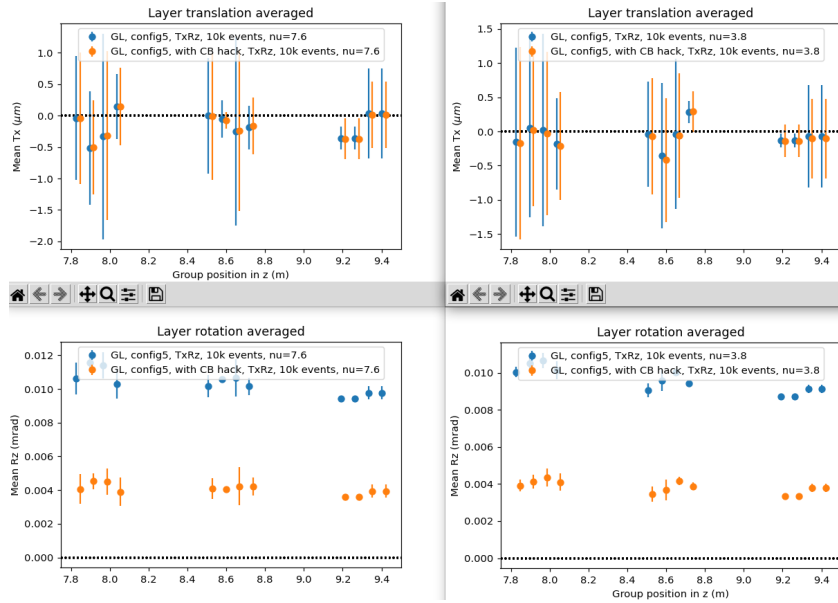


Abbildung 4.20: Impact of the clusterbias for high and low luminosity samples.

better behaved in station 2 when looking at x-translation. Regarding the z-rotation, the lower luminosity sample as slightly lower rotational shifts. The difference is so minute that it can be safely disregarded. (not sure about that)

With that, we tested if there is a noticable difference in the  $\frac{\chi^2}{\text{dof}}$  and the result is shown in figure 4.22.

Now, since the alignment works quite good with the current configuration we tested how translation misalignment effects the convergence by looking at the  $\chi^2$ , portrayed in figure 4.23. For this figure, eight different samples of 100  $\mu\text{m}$  module translation misalignment over all translatory degrees of freedom. The idea behind using different samples is to reduce errors from biased samples. The plot shows the total  $\chi^2$  over degrees of freedom plotted against the number of iterations. We see no visible difference regarding the total  $\chi^2$  between the samples which is good. Also, the total  $\chi^2$  decreases with an increasing number of iterations during the alignment.

We do want the least amount of constraints in the system so we also tested the consequences of removing constraints from "config5". The results are shown in figure 4.24. The green curve shows the base config for comparison and in red the removal of the backlayer constraint in station 3 is shown. The blue curve shows the alignment results without the C-frame constraints. The data samples used were from 2020 with the normal luminosity and an active clusterbias hack. The selected track types

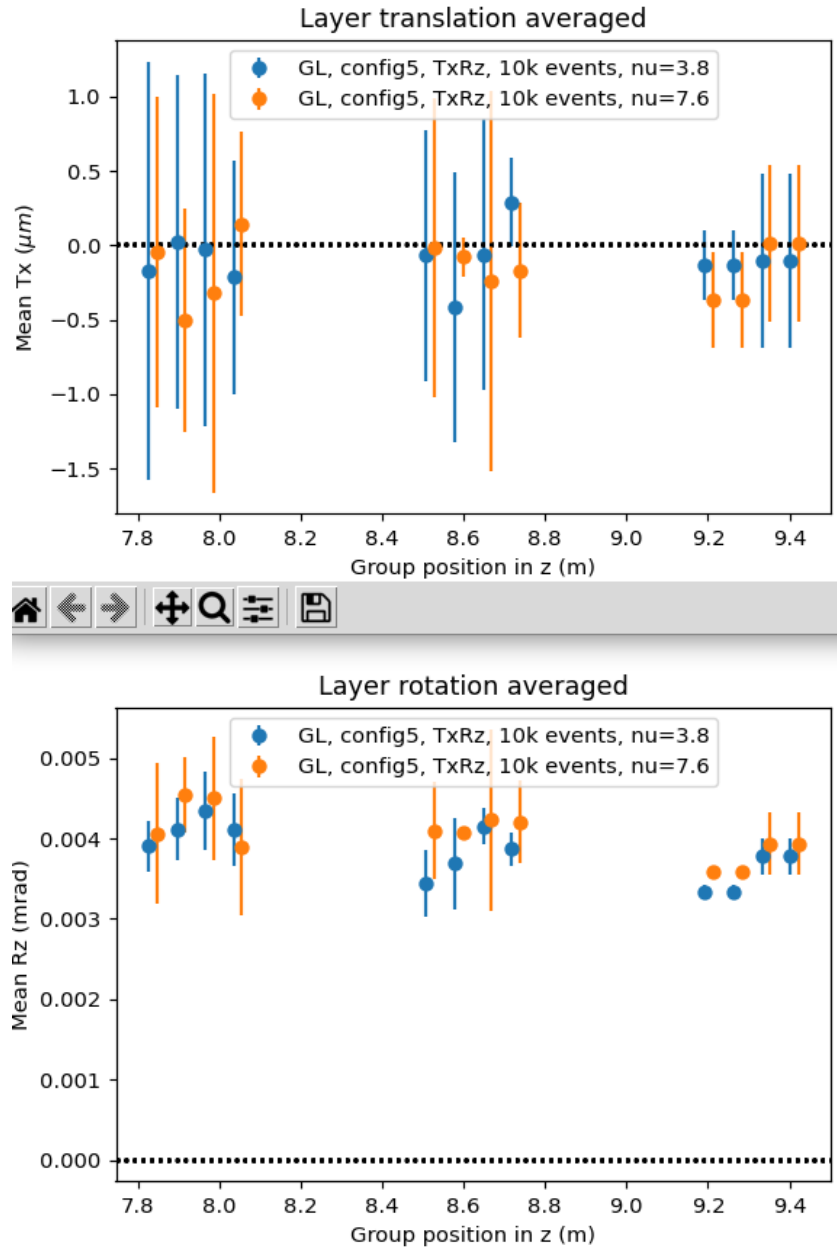


**Abbildung 4.21:** show difference between low and normal luminosity with clusterbias hack active.



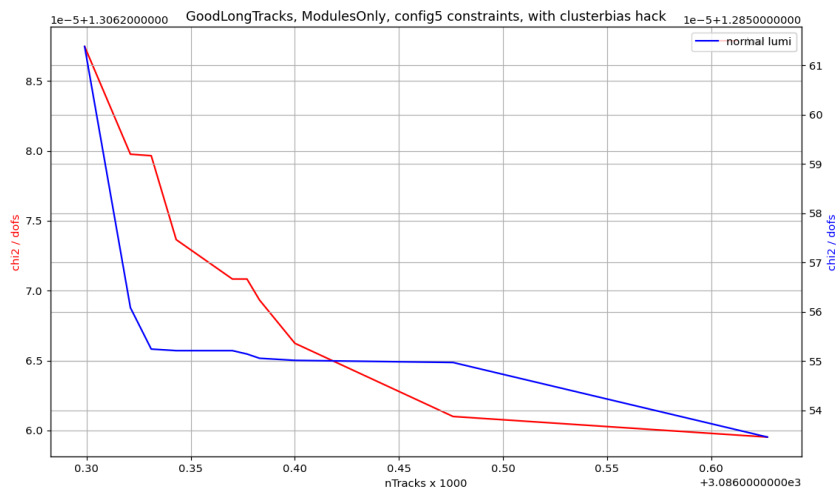


**Abbildung 4.22:** GoodLong tracks for module alignment and config 5 active. also the clusterbias hack is active comparing low and normal luminosity.

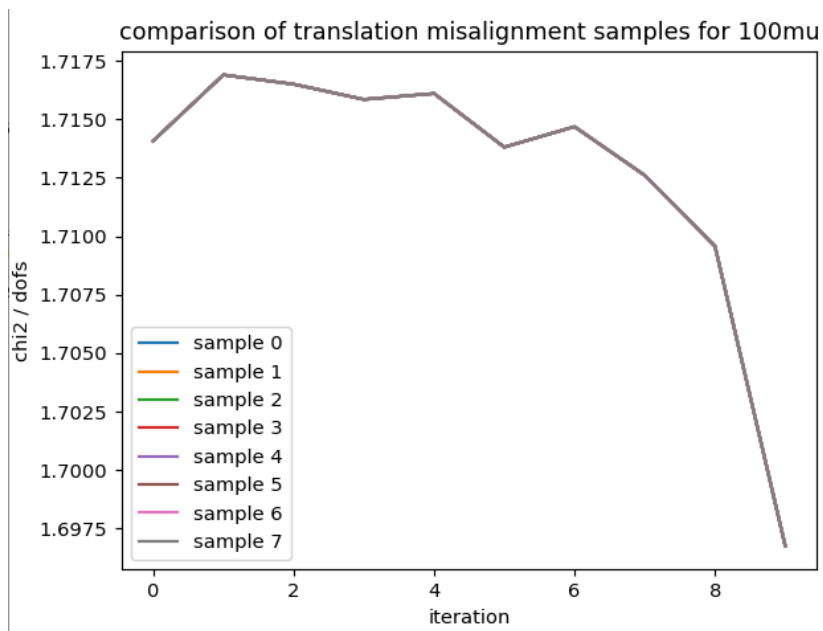


**Abbildung 4.23:** 100mu translation misalignment comparison for different misalignment samples.

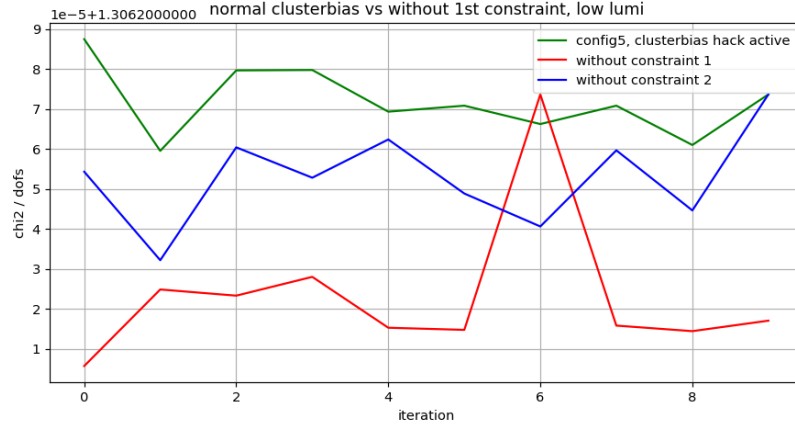


**Abbildung 4.24:** impact of removing constraints from existing studies regarding  $\chi^2$ .

are *HighMomentumTTracks*(?) for 10000 events (?). On the one hand we see an improvement in  $\chi^2/\text{dof}$  when removing these constraints individually even if it is only on a very small scale of  $1 \cdot 10^{-5}$ . On the other hand we see that the  $\chi^2/\text{dof}$  after the last iteration is the same for the base config and for the blue measurement. The constraint removed in the red measurement seems to have the most impact from what was tested but the peak in iteration 6 has no logical explanation for now. Additional analysis regarding constraint removal will be done in the future to analyse this phenomenon further. Also the behavior of the not decreasing  $\chi^2/\text{dof}$  requires more testing. What can be taken from this is that the removal of some constraints will help the alignment but the cause of some abnormalities require more testing.

## 5 Continuing Work

## 6 Future Work

instead of only doing normal(low) luminosity tests do it for the other luminosity as well (jan 24th)

## 7 Conclusion and Outlook

## Literatur

- [1] *A diagram showing the complete structure of the LHC facility at CERN.* URL: [https://www.researchgate.net/figure/A-diagram-showing-the-complete-structure-of-the-LHC-facility-at-CERN-There-are-the-4\\_fig8\\_348806406](https://www.researchgate.net/figure/A-diagram-showing-the-complete-structure-of-the-LHC-facility-at-CERN-There-are-the-4_fig8_348806406) (besucht am 09.03.2022).
- [2] *A sideview showing the LHCb detector's main elements.* URL: <https://cerncourier.com/a/lhcb-momentous-metamorphosis/> (besucht am 09.03.2022).
- [3] *Alignment.* URL: <https://gitlab.cern.ch/lhcb/Alignment> (besucht am 21.04.2022).
- [4] *b-hadron production at LHCb.* URL: <https://cds.cern.ch/record/2206834/files/LHCb-TALK-2016-222.pdf> (besucht am 20.04.2022).
- [5] Matteo Cacciari, Mario Greco und Paolo Nason. „The P(T) spectrum in heavy flavor hadroproduction“. In: *JHEP* 05 (1998), S. 007. eprint: hep-ph/9803400. URL: <https://arxiv.org/pdf/hep-ph/9803400.pdf>.
- [6] Sophie Hollitt. *Current topics in SciFi Alignment.* URL: <https://indico.cern.ch/event/997932/contributions/4263653/attachments/2206615/3733618/SciFiAlignOverview-11-03.pdf> (besucht am 20.04.2022).
- [7] *LHC Machine.* URL: [https://cds.cern.ch/record/1129806/files/jinst8\\_08\\_s08001.pdf](https://cds.cern.ch/record/1129806/files/jinst8_08_s08001.pdf) (besucht am 09.03.2022).
- [8] *LHCb Tracker Upgrade Technical Design Report.* URL: <https://cds.cern.ch/record/1647400/files/LHCB-TDR-015.pdf> (besucht am 09.03.2022).
- [9] *Physical Constants.* URL: <http://pdg.lbl.gov/2019/mobile/reviews/pdf/rpp2018-rev-phys-constants-m.pdf> (besucht am 11.08.2019).
- [10] Florian Reiss. *Update on VP alignment constraint issue.* URL: [https://indico.cern.ch/event/997937/contributions/4369419/attachments/2248454/3813923/WP45\\_FReiss\\_20210520.pdf](https://indico.cern.ch/event/997937/contributions/4369419/attachments/2248454/3813923/WP45_FReiss_20210520.pdf) (besucht am 21.04.2022).
- [11] *standard Model.* URL: <https://www.physik.uzh.ch/en/researcharea/lhcb/outreach/StandardModel.html> (besucht am 11.04.2022).
- [12] *The invariant Rauch-Tung-Striebel Smoother.* URL: <http://ras.papercept.net/images/temp/IROS/files/2526.pdf> (besucht am 24.03.2022).

- [13] *The LHCb Detector at the LHC*. URL: [https://cds.cern.ch/record/1129809/files/jinst8\\_08\\_s08005.pdf](https://cds.cern.ch/record/1129809/files/jinst8_08_s08005.pdf) (besucht am 09.03.2022).
- [14] Prof. Mark Thomson. *Particle Physics*. URL: [https://www.hep.phy.cam.ac.uk/~thomson/lectures/partIIIparticles/Handout8\\_2009.pdf](https://www.hep.phy.cam.ac.uk/~thomson/lectures/partIIIparticles/Handout8_2009.pdf) (besucht am 13.04.2022).
- [15] J Van Tilburg. „Track simulation and reconstruction in LHCb“. Presented on 01 Sep 2005. 2005. URL: <https://cds.cern.ch/record/885750>.

## Danksagung

An dieser Stelle möchte ich mich bei all denen bedanken, die mir während meiner Bachelorarbeit zur Seite standen und mich immer unterstützt haben.

Zuerst möchte ich mich bei Herrn Professor Dr. Kevin Kröninger bedanken, durch welchen ich an seinem Lehrstuhl meine Bachelorarbeit schreiben konnte. Außerdem möchte ich mich bei der Abteilung der ATLAS Datenanalyse für die konstruktiven Anregungen bedanken.

Einen großen Dank spreche ich vor allem meinem Betreuer Dr. Johannes Erdmann aus, der mich mit voller Unterstützung und wertvollen Ratschlägen und Hilfestellungen durch meine Bachelorarbeit begleitet hat. Durch ihn habe ich viel gelernt und bei Fragen konnte er mir stets weiterhelfen.

Ich möchte mich auch bei Herrn Professor Dr. Bernhard Spaan für die Zweitkorrektur meiner Arbeit bedanken.

Mein Dank gebührt außerdem Christopher Krause, Jan Lukas Späh, Michael Windau, Sebastian Lütge und Christian Beckmann für die fachliche Kompetenz bei Fragen aller Art.

Zuletzt möchte ich meiner Familie und Freunden dafür danken, dass sie mich während meines gesamten Studiums immer unterstützt und motiviert haben.



## Eidesstattliche Versicherung

Ich versichere hiermit an Eides statt, dass ich die vorliegende Abschlussarbeit mit dem Titel „Alignment studies for the LHCb SciFi Detector“ selbstständig und ohne unzulässige fremde Hilfe erbracht habe. Ich habe keine anderen als die angegebenen Quellen und Hilfsmittel benutzt, sowie wörtliche und sinngemäße Zitate kenntlich gemacht. Die Arbeit hat in gleicher oder ähnlicher Form noch keiner Prüfungsbehörde vorgelegen.

---

Ort, Datum

---

Unterschrift

## Belehrung

Wer vorsätzlich gegen eine die Täuschung über Prüfungsleistungen betreffende Regelung einer Hochschulprüfungsordnung verstößt, handelt ordnungswidrig. Die Ordnungswidrigkeit kann mit einer Geldbuße von bis zu 50 000,00 € geahndet werden. Zuständige Verwaltungsbehörde für die Verfolgung und Ahndung von Ordnungswidrigkeiten ist der Kanzler/die Kanzlerin der Technischen Universität Dortmund. Im Falle eines mehrfachen oder sonstigen schwerwiegenden Täuschungsversuches kann der Prüfling zudem exmatrikuliert werden (§ 63 Abs. 5 Hochschulgesetz –HG–).

Die Abgabe einer falschen Versicherung an Eides statt wird mit Freiheitsstrafe bis zu 3 Jahren oder mit Geldstrafe bestraft.

Die Technische Universität Dortmund wird ggf. elektronische Vergleichswerkzeuge (wie z. B. die Software „turnitin“) zur Überprüfung von Ordnungswidrigkeiten in Prüfungsverfahren nutzen.

Die oben stehende Belehrung habe ich zur Kenntnis genommen.

---

Ort, Datum

---

Unterschrift